Low-Profile, Electrically Small, Ultra-Wideband Antenna Enabled with an Inductive Grid Array Metasurface

Qingli Lin, Ming-Chun Tang, Xiaoming Chen, Da Yi, Mei Li, and Richard W. Ziolkowski

***Abstract*—A low-profile, electrically small, ultra-wideband (UWB) antenna enabled with a grid array metasurface is presented. The design incorporates a driven dipole, an electric near-field resonant parasitic (NFRP) element, and a grid array structure which operates as an inductive metasurface. The NFRP element is an Egyptian axe dipole (EAD) that is excited by the driven dipole. This combination itself is an electrically small NFRP dipole antenna. In contrast to previous versions, its operation in both its first and third resonant modes is established. The presence of the grid, which consists of identical interconnected rectangular loops, then provides a new dipole mode and facilitates the reduction of the frequency ratio of the NFRP dipole's modes. The resulting overlap of these three resonant modes yields the UWB operation. The electrically small (*ka* = 0.92), low profile (0.003 λ_0) antenna exhibits uniform radiation patterns and stable and high radiation efficiency performance characteristics. The antenna was optimized, fabricated, and tested. The measured results, in good agreement with their simulated values, demonstrate that the antenna yields a ultra-wide, 67.7%, –10-dB impedance bandwidth with stable realized gain values, ~ 1.6 dBi, and high radiation efficiency (RE) values, RE > 77%, over its entire operational bandwidth.**

***Index Terms* — Electrically small antennas, grid array antennas (GAAs), inductive metasurface, low-profile, near-field resonant parasitic (NFRP) elements, ultra-wideband (UWB).**

I. Introduction

Grid array antennas (GAAs), composed of a periodic grid of cells, hold a variety of advantages. These include broad bandwidths, high gain values, compact sizes, low profiles, simple feed structures, and adequate cross polarization level control abilities. Since Kraus proposed the first GAA in 1964 [1], various international teams have developed GAAs [2]-[22]. For example, several types of GAAs have been designed to enhance the impedance and gain bandwidths. They include employing elliptical [6] and rhombic [7] radiation elements; loading the radiation lines with reactive disk elements [8]; decreasing the long lines at the radiator edges [9]; and adopting astroid cell structures [11]. Moreover, several methods have been reported to reduce the electric size of a GAA. For instance, the traditional straight transmission lines were replaced with sinusoidal lines to accomplish an area-reduction factor of 47% [6]. Loop elements [12] have been employed successfully to achieve a 57% size reduction in comparison to the standard rectangular grid counterpart. Furthermore, GAAs have been reported for several different advanced wireless platforms, e.g., millimeter-wave communications [14]-[19]; wearable and epidermal [20]; and multi-function [21], [22] systems.

Manuscript received June 30, 2021; revised October 18, 2021; and accepted January 18, 2022. This work was supported in part by the National Natural Science Foundation of China contract number 62031006, in part by the Chongqing Natural Science Foundation contract number cstc2019jcyjjqX0004, and in part by the Australian Research Council grant number DP160102219. *(Corresponding author: Ming-Chun Tang.)*

Q. Lin, M. -C. Tang, X. Chen, D. Yi, and M. Li are with the Key Laboratory of Dependable Service Computing in Cyber Physical Society Ministry of Education, School of Microelectronics and Communication Engineering, Chongqing University, Chongqing 400044, China (e-mail: tangmingchun@cqu.edu.cn);

R. W. Ziolkowski is with the University of Technology Sydney, Global Big Data Technologies Centre, Ultimo NSW 2007, Australia (e-mail: richard.ziolkowski@uts.edu.au).

While one might easily conclude that GAAs are a well-established technology, most reported GAAs that achieve large impedance bandwidths come at the cost of being electrically large [6]-[11]. To the best of our knowledge, there have been no electrically small GAA versions reported to date, i.e., none with their $ka < 1$, where $k = 2\pi/\lambda_0 = 2\pi f_L/c$ is the free-space wave number corresponding to the lower bound of the operational band, f_L, and a is the radius of the smallest sphere that completely encloses the entire antenna system.

In this Communication, an electrically small ultra-wideband (UWB) GAA is developed. The GAA is composed of a driven dipole, a near-field resonant parasitic (NFRP) Egyptian axe dipole (EAD) element [23-25], and a grid array structure consisting of 32 rectangular grid cells in a 7×5 configuration. The proposed grid cells are composed of strips with unequal widths. The grid produces a strong inductance effect and, hence, acts as an inductive metasurface located in the near field of the antenna system. Consequently, its function is quite different from the transmission-line grids in the reported GAAs [2]-[22]. The presence of the inductive grid structure not only reduces the ratio of the first- and third-order modes of the NFRP element, but it also contributes a new resonance mode which overlaps the original two. As a consequence, a UWB operation is attained. The radiation patterns are stable and the system achieves high radiation efficiency over the entire operational bandwidth.

We note that a Yagi-configured, polarization-reconfigurable, electrically small antenna (ESA) was reported in [26] that was based on cross-shaped EAD NFRP elements. Four p-i-n (PIN) diodes were integrated into the driven element; their ON-OFF states facilitated four independent polarization states within a narrow overlapping operational bandwidth. While this paper also employs an EAD-based electrically small antenna, its augmentation with a passive grid-based metasurface to achieve a GAA is an entirely different concept. In fact, it is a UWB system and is not reconfigurable. Moreover, while the EAD-based system in [26] operated in the fundamental mode of the EAD element, its first and third modes are employed here.

This paper is organized as follows. The antenna design is introduced in Section II. The optimized prototype that was fabricated and tested is described in Section III. The measured results are shown to be in good agreement with their simulated values. Finally, some conclusions are drawn in Section IV.

We note that all of the metallic elements modeled in the antenna designs were chosen to be copper with its known material parameters: $\varepsilon_r = 1.0$, $\mu_r = 0.999991$ and bulk conductivity $\sigma = 5.8 \times 10^7$ Siemens/m. All of the numerical electromagnetic simulations and their optimizations were performed using the frequency domain, finite element-based ANSYS/ANSOFT High Frequency Structure Simulator (HFSS), version 2021. The circuit simulations were performed with the Agilent Advanced Design System (ADS).

II. Antenna Design

A. Electrically Small UWB GAA Configuration

The configuration of the developed electrically small UWB GAA is shown in Fig. 1. As shown in Figs. 1(a) and 1(b), it consists of two

substrate layers that are labeled as Layer_1 and Layer_2. Both substrate layers are the Rogers Duroid™ 5880 board material with relative dielectric constant ε_r = 2.2, loss tangent *tan* δ = 0.0009, and copper cladding thickness H_1 = 0.017 mm. The two layers have the same radius, R_1 = 35.0 mm, and the same thickness, H_2 = 0.127 mm. As is shown in Fig. 1(a), the grid structure consists of 32 rectangular loops printed on the upper surface of Layer_1. The NFRP EAD with a gap introduced at its center is printed on the lower surface of Layer_1. The driven dipole is printed on the bottom of the Layer_2 and is excited across its center gap.

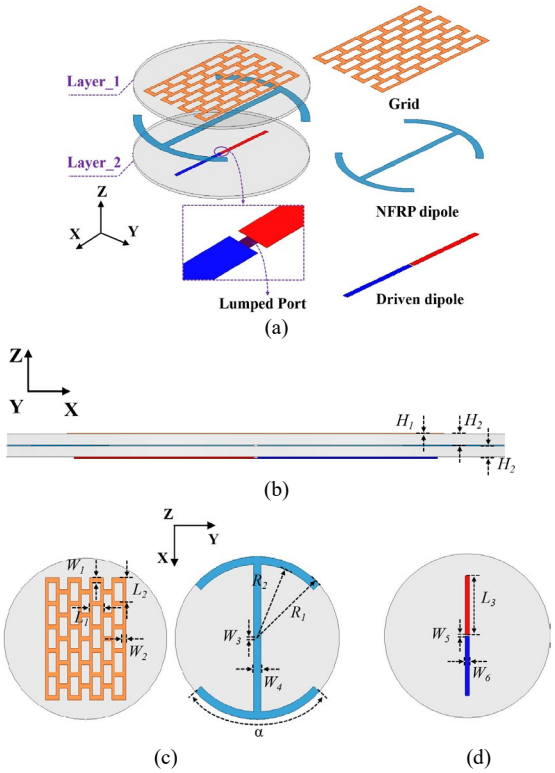

Fig. 1 Configurations of the developed electrically small UWB GAA. (a) 3-D isometric view. (b) Side view. (c) Upper and lower surfaces of Layer_1. (d) Lower surface of Layer_2.

The configurations of the grid structure and the NFRP EAD are depicted in Fig. 1(c). The grid structure consists of 32 rectangular grid cells with the same dimensions, but in a staggered arrangement. The lines of four cells are centered on the five cell ones. The lengths of the short side and the long side of each unit cell are, respectively, L_1 and L_2. The corresponding widths of the short and long sides are, respectively, W_1 and W_2. The resonance frequency of the grid element is determined by these and its consequent overall dimensions. The NFRP EAD is placed directly below the grid structure and is centered with respect to its center-line. Its straight strips are oriented parallel to the long side of the grid. The gap etched at the center of the NFRP dipole is W_3 in length. Its presence effectively helps excite the resonance mode of the grid structure. The fundamental and higher modes of the EAD are mainly determined by the EAD's total length [23]-[25]. The presence of the grid not only introduces a resonance between the EAD's fundamental and third order resonances, but it also significantly lowers the ratio of their frequencies.

The driven dipole is shown in Fig. 1(d). The length of each half and their widths are L_3 and W_6, respectively. To simplify the initial simulations, a lumped port was set at the center of the driven dipole. The optimized design parameters are given in Table I.

TABLE I

OPTIMIZED DESIGN PARAMETERS OF THE DEVELOPED ELECTRICALLY SMALL UWB GAA (DIMENSIONS IN MILLIMETERS)

H_1 = 0.017	H_2 = 0.127	W_1 = 1.96	W_2 = 1.28	W_3 = 0.5
W_4 = 3.08	W_5 = 0.5	W_6 = 1.56	L_1 = 6.02	L_2 = 10.2
L_3 = 25.16	R_1 = 35.0	R_2 = 31.6	α = 98.0°	*NULL*

B. Equivalent Circuit Model

An equivalent circuit model was developed to provide a comprehensive explanation of the operating mechanisms of our electrically small GAA. Note that because of the symmetry of the antenna with respect to the *z0y*-plane, an electrical wall is introduced in it to simplify the circuit model. According to the periodic structure analysis in [27], our grid structure acts as an inductive impedance surface when the polarization of the incident wave is aligned along its long strips. Consequently, each of its unit cells can be represented by a series of inductors whose values are simply calculated as [28]

$$L = \frac{\mu_0 l}{2\pi}\left(\ln\frac{2l}{w+t}+0.5\right) \tag{1}$$

where L indicates the inductance of one of its metal strips whose width, length, and thickness are, respectively, w, l, and t. Note that the mutual inductance between the unit cells of the grid is quite low in comparison to its own self-inductance. Thus, it is ignored in the circuit model [29]. A complete unit grid cell and its equivalent circuit model are shown in Fig. 2. The inductances of the long and short sides of this cell are represented by *L_long* and *L_short*, respectively. The capacitive coupling between the two long adjacent sides is modeled as the capacitance *C_short*.

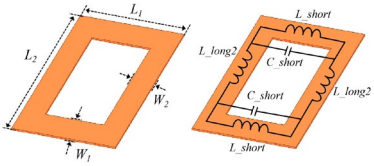

Fig. 2 A typical grid cell and its equivalent circuit model.

The equivalent circuit model of the NFRP EAD ESA alone has been detailed previously [30]. However, the EAD element in the GAA is capacitively coupled to the periodic sections of the grid. Therefore, the inductances and capacitances associated with those sections should be represented separately in the equivalent circuit model. It is well known that a dipole antenna can be considered as a transmission line with radiation characteristics [31]. Therefore, the overlapping sections of both the driven and NFRP elements are divided into 5 parts whose inductances are represented by *L_driven* and *L_NFRP*, respectively. The non-overlapping straight section of the EAD is approximately equivalent to an inductor *L_NFRP*, and its top hat structure is equivalent to an inductor *L_hat*. The coupling between the NFRP element and infinity is represented by a capacitor *C_hat*. The values of *L_driven* and *L_NFRP* are also calculated with Eqn. (1). The gap at the middle of the NFRP dipole is represented by the capacitor *C_gap*. The capacitive coupling between the driven and parasitic dipoles is represented by *C_dipole*. Since the middle column of the grid is directly located above the NFRP dipole, 5 pairs of capacitors (*C_couple*) are utilized to represent the coupling between the edges of the center strips of the NFRP element and the nearest strips of the two five cell lines of the grid nearest the center line. Since the resonant modes of this antenna arise from the combination of the NFRP element and the grid, the radiation resistance (*R_rad*) is associated with the currents flowing on it. Finally, the capacitive coupling between the whole antenna and infinity is represented by *C_gnd*.

The entire equivalent circuit model of our GAA is shown in Fig. 3(a). The extracted values of the various lumped elements in the equivalent circuit model after they have been optimized from their initial approximate values to those which fully duplicate the HFSS simulation results are listed in Table II.

TABLE II

THE VALUES OF THE LUMPED ELEMENTS IN THE EQUIVALENT CIRCUIT MODEL OF THE DEVELOPED UWB GAA

L_long = 3.48 nH	*L_long2* = 6.97 nH	*L_short* = 1.25 nH
L_driven = 2.2 nH	*L_NFRP* = 1.7 nH	*L_hat* = 9.6 nH
C_dipole = 0.269 pF	*C_couple* = 0.125 pF	*C_hat* = 0.61 pF
C_short = 0.01 pF	*C_gnd* = 0.001 pF	*R_rad* = 76.0 Ω
C_gap = 6.0 pF	*NULL*	

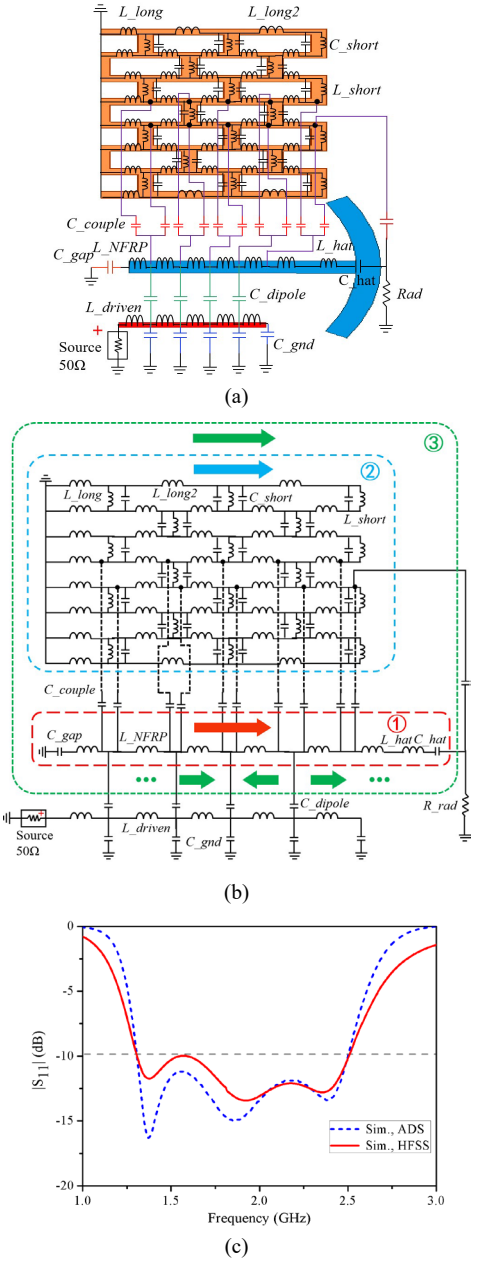

Fig. 3 UWB GAA. (a) Equivalent circuit model. (b) The corresponding resonant modes. (c) Comparison of the ADS and HFSS simulated $|S_{11}|$ values as functions of the source frequency.

The groups of circuit components associated with the three resonant modes of the NFRP element and the grid structure are indicated in Fig. 3(b) and are labeled as ①, ② and ③. The corresponding current directions are also shown. The red dashed box indicates the equivalent circuit pieces tied with resonant mode ① of the NFRP element. The induced current direction is highlighted by the red arrow. Similarly, the blue dashed box labeled ② indicates the circuit components associated with the resonant mode of the grid structure. The blue arrow represents its current direction. The circuit elements associated with the higher-order mode that arises from the NFRP element and grid combination are encompassed in the green dashed box and are labeled ③. The current directions associated with mode ③ are highlighted with the green arrows.

The simulated reflection coefficients ($|S_{11}|$) obtained from the equivalent circuit model with ADS and with the HFSS model of the GAA are presented and compared in Fig. 3(c). The resonance frequencies and the impedance bandwidth obtained with the two simulation approaches are basically coincident. This outcome confirms the effectiveness of the equivalent circuit model. Moreover, these results clearly indicate the presence of three resonance modes. Their overlapping nature gives rise to the ultra-wide bandwidth of the GAA.

C. Surface Current Distributions

The operating mechanisms of the three resonant modes of the GAA are illustrated with the current distribution behaviors on the NFRP EAD element and grid array structure and the resulting 3-D realized gain patterns at the resonance frequencies 1.4, 1.9 and 2.4 GHz in Figs. 4(a)–4(c), respectively.

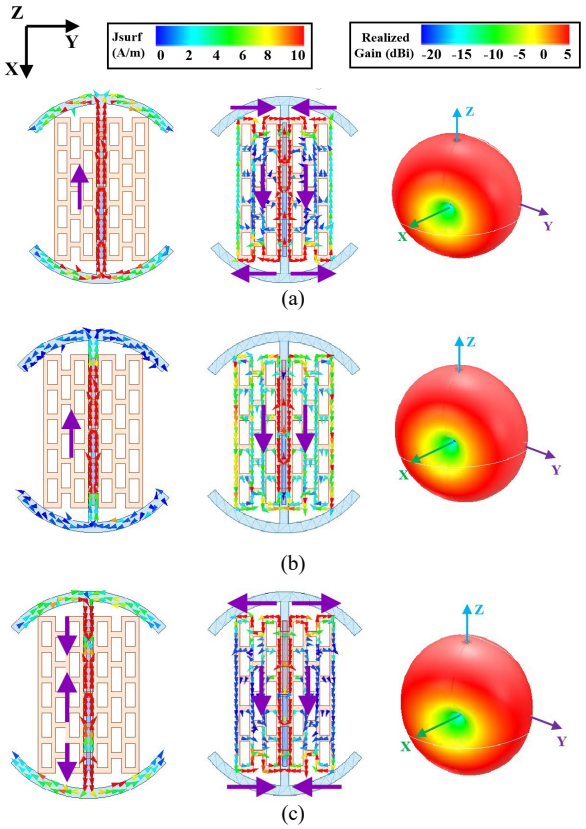

Fig. 4 Surface current distributions on the NFRP EAD element and on the grid structure of the developed UWB GAA and the resulting 3-D realized gain patterns at its resonance frequencies. (a) 1.4 GHz. (b) 1.9 GHz. (c) 2.4 GHz.

The prominent current directions are highlighted with the purple arrows. As shown in Fig. 4(a), the currents on the EAD element are uniformly distributed along its center strips in the *x*-axis direction. As confirmed by the 3-D pattern, the GAA is operating in its fundamental dipole mode at this lowest resonance frequency, 1.4 GHz [32].

Similarly, the surface currents in Fig. 4(b) associated with the second mode are mainly on the grid structure and are oriented along its long side, also parallel to the *x*-axis. The 3-D pattern at 1.9 GHz clearly shows that the resonance of the grid structure is also radiating in its fundamental dipole mode. The current distributions on the EAD element in Fig. 4(c) at the third resonance frequency clearly indicate that it is operating in a higher order mode (HoM). However, the resonant currents on the grid structure combine with those of the HoM to form a third dipole mode. The 3-D pattern at 2.4 GHz confirms this behavior.

Our simulation studies have further demonstrated that the currents present on the top-hat curved arcs at the two ends of the EAD element and on the driven dipole also contribute to the formation of this third dipole mode, as was reported in [33]. Finally, simulations of the dipole excited EAD element and excited grid structure alone demonstrate that the introduction of the grid structure narrows the frequency ratio of the first- and third-order modes while the resonance frequency of the grid structure occurs between theirs. The resulting overlap of these three resonant modes yields the UWB operation.

III. Simulated and Measured Results

The electrically small UWB GAA was fabricated, assembled, and measured. Recall that a lumped port was used in the simulations as the 50 Ω source to excite it. In the measurements, the actual transition from the coax-line cable of the network analyzer to the unbalanced driven dipole had to be considered. A UWB balun was designed and implemented to significantly decrease the influence of the leakage currents on the outer wall of the cable [34]. This exponentially-tapered microstrip to parallel strip structure is much simpler than a sleeve balun and has a much wider operational bandwidth [35].

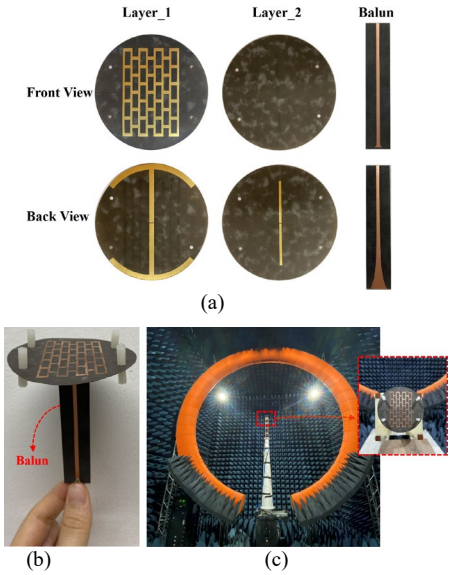

Fig. 5 Fabricated UWB GAA. (a) Front and back views of each layer before assembly. (b) 3-D isometric view. (c) The AUT in the anechoic chamber.

The component parts before assembly are presented in Fig. 5(a). The assembled antenna with the UWB balun is shown in Fig. 5(b). The S-parameters of the developed GAA were measured with an Agilent E8361A PNA vector network analyzer (VNA). The far-field realized gain (RG) pattern and radiation efficiency (RE) were measured with an SG128 multi-probe antenna measurement system at the China Academy of Information and Communications Technology, Chongqing, China [36]. The antenna under test (AUT) in the measurement chamber is shown in Fig. 5(c).

The measurement of the transmission characteristics of the UWB balun were carried out first. Its measured and simulated S-parameters are compared in Fig. 6. The measured (simulated) bandwidth, where $|S_{11}| \le -15$ dB, covered more than the entire L- and S-bands, i.e., it was > 1–4 GHz. Within this frequency range, the measured (simulated) transmission coefficient is better than –1.1 (–0.3) dB and, hence, provides a low transmission loss.

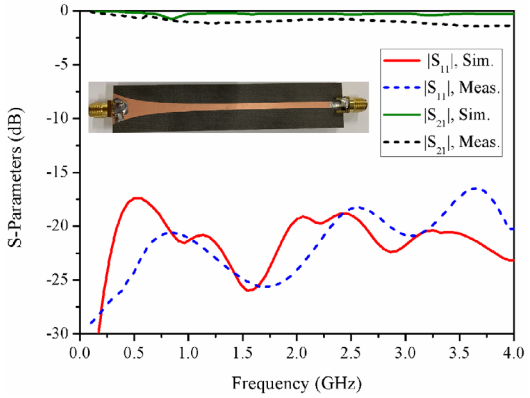

Fig. 6 Simulated and measured S-parameters of the developed UWB balun as functions of the source frequency.

The simulated and measured $|S_{11}|$ values of the UWB GAA are shown in Fig. 7. The simulated (measured) –10-dB impedance bandwidth (highlighted in yellow) is 63.1%, from $f_L = 1.31$ to $f_H = 2.52$ GHz (67.7%, from 1.26 to 2.55 GHz), i.e., $2(f_H–f_L)/(f_H+f_L) > 0.25$ which by definition is UWB [37], [38]. The simulated (measured) electrical size of the total antenna system is $ka = 0.95$ (0.92). Three resonant dips are readily observed. Their minimums are located at 1.4 (1.42), 1.9 (1.88), and 2.4 (2.42) GHz. The UWB operation is confirmed.

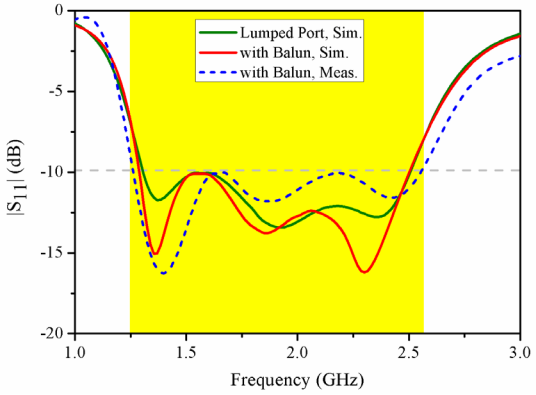

Fig. 7 Simulated and measured $|S_{11}|$ values of the developed UWB GAA as functions of the source frequency. The impedance bandwidth is highlighted in yellow.

The simulated and measured peak realized gain values of the UWB GAA are plotted in Fig. 8. The simulated (measured) realized gain values are maintained around 2.2 dBi (1.6 dBi) with a gain fluctuation within 0.8 dBi (0.8 dBi) over the entire operational bandwidth. The

simulated (measured) maximum gain fluctuations with respect to all directions in the H-plane are also presented over these frequencies. They are less than 2.8 dB (3.1 dB). Thus, the GAA has a stable omnidirectional radiation pattern over its entire operational bandwidth. The simulated and measured RE results shown in Fig. 9 demonstrate that the simulated (measured) overall efficiencies values are larger than 85% (77%) over the same bandwidth.

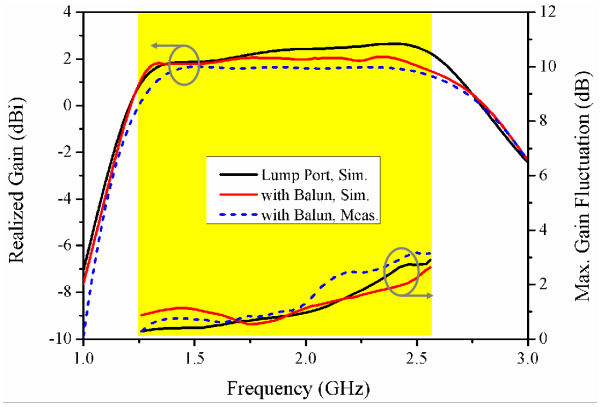

Fig. 8 Simulated and measured RG values, and the maximum gain fluctuation with respect to all directions in the H-plane of the developed UWB GAA as functions of the source frequency. The impedance bandwidth is highlighted in yellow.

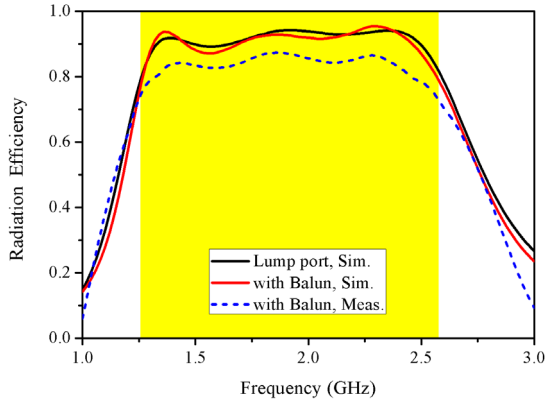

Fig. 9 Simulated and measured overall efficiency values of the developed UWB GAA as functions of the source frequency. The impedance bandwidth is highlighted in yellow.

The simulated and measured normalized realized gain patterns at the noted three resonance frequencies are displayed in Figs. 10(a)–10(c). One clearly observes that the UWB GAA exhibits uniform omni-directional performance within the entire operational bandwidth. Moreover, the simulated and measured cross-polarization levels are lower than –20 dB. In general, the simulated results are in quite good agreement with their measured values.

Table III provides a comparison between the UWB GAA prototype and recently reported wideband dipole antennas [39]-[42]. It is clearly observed that our prototype realized a considerably wider bandwidth (67.7%) despite being electrically small in size (ka < 1). On the other hand, its relatively smaller peak realized gain in comparison to the systems in [39]-[41] is a direct consequence of it being electrically and physically smaller than they are. Nevertheless, our GAA has demonstrated stable omnidirectional radiation patterns over its entire, much wider operational bandwidth.

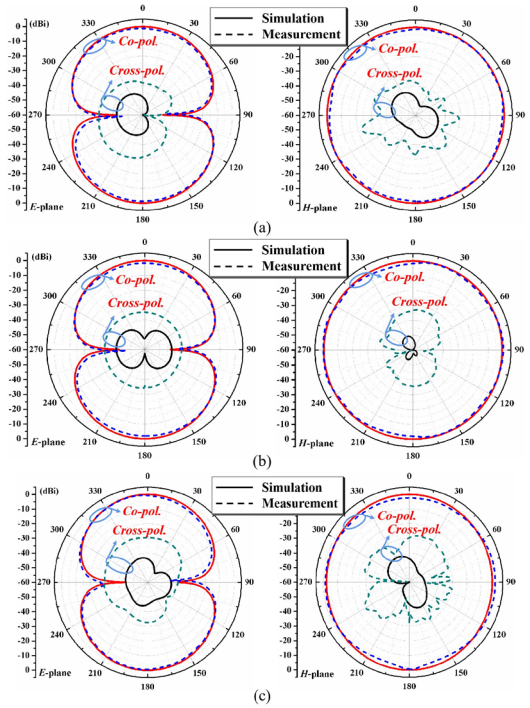

Fig. 10 The simulated and measured normalized realized gain patterns of the UWB GAA prototype operating at (a) 1.4 GHz in simulation and 1.42 GHz in measurement, (b) 1.9 GHz in simulation and 1.88 GHz in measurement, and (c) 2.4 GHz in simulation and 2.42 GHz in measurement.

TABLE III
PERFORMANCE COMPARISON OF THE PROTOTYPE GAA WITH RECENTLY REPORTED DIPOLE ANTENNAS

Refs.	ka	Physical Size (λ_0^3)	$\|S_{11}\|$ BW (%)	Peak Real. Gain (dBi)
[39]	1.73	$0.49\times0.24\times0.0049 = 5.76\times10^{-4}$	44.2	4.6
[40]	4.26	$1.07\times0.83\times0.014 = 0.012$	~1.9	4.6
[41]	3.93	$0.99\times0.79\times0.014 = 0.011$	8.6	4
[42]	1.01	$0.32\times0.03\times0.01 = 9.6\times10^{-5}$	~19.5	1.9
GAA	0.92	$3.14\times(0.15)^2\times0.003 = 2.12\times10^{-4}$	67.7	2.6

IV. CONCLUSION

A low-profile, electrically small, UWB GAA was presented. The GAA is composed of a driven dipole, a NFRP EAD, and a grid structure. The NFRP element operates in its first and third resonant modes. The presence of the grid structure provides a third resonance whose frequency falls between the two EAD resonance frequencies. Not only does it cause the resonance frequency of the higher order mode of the EAD to decrease while leaving that of the fundamental mode the same (hence, the ratio of its resonance frequencies is decreased by its presence), the currents on the grid structure at the highest resonance frequency compensate for those on the EAD so that the overall currents radiate in an electric dipole sense. Thus, the EAD-grid combination not only produces three overlapping resonance modes which yield the UWB operation, but it also facilitates a system that radiates as an electric dipole with very stable realized gain patterns across its entire ultra-wide band.

A prototype of the optimized design was fabricated and tested. It was very low profile (height ~ $0.003\lambda_0$) and electrically small (ka = 0.92 < 1). The measured results, in good agreement with their

simulated values, demonstrated that the antenna yields an ultra-wide, 67.7% impedance bandwidth with stable realized gain values, ~ 1.6 dBi, and high RE values, RE > 77 %, over its entire operational bandwidth. With these advantageous performance characteristics it is an attractive candidate for many current and future wideband space-limited wireless communication platforms associated, for example, with WiMax, Wi-Fi, and fifth-generation (5G) mobile networks.

REFERENCES

[1] J. Kraus, "A backward angle-fire array antenna," *IEEE Trans. Antennas Propag.*, vol. 12, no. 1, pp. 48–50, Jan. 1964.

[2] R. Conti, J. Toth, T. Dowling, and J. Weiss, "The wire grid microstrip antenna," *IEEE Trans. Antennas Propag.*, vol. 29, no. 1, pp. 157–166, Jan. 1981.

[3] H. Nakano, I. Oshima, H. Mimaki, K. Hirose, and J. Yamauchi, "Center-fed grid array antennas," in *Proc. 1995 IEEE Antennas and Propagation Society International Symposium*, Newport Beach, CA, USA, pp. 2010–2013, Jun. 1995.

[4] H. Nakano, T. Kawano, and J. Yamauchi, "Meander-line grid-array antenna," *IET Microw. Antennas Propag.*, vol. 145, no. 4, pp. 309–312, Aug. 1998.

[5] H. Nakano, T. Kawano, and J. Yamauchi, "A cross-mesh array antenna," in *Proc. 2001 Eleventh International Conference on Antennas and Propagation*, *(EICAP 2001)*, Manchester, England, pp. 327–330, Apr. 2001.

[6] X. Chen, G. Wang, and K. Huang, "A novel wideband and compact microstrip grid array antenna," *IEEE Trans. Antennas Propag*., vol. 58, no. 2, pp. 596–599, Feb. 2010.

[7] H. Nakano, Y. Iitsuka, and J. Yamauchi, "Rhombic grid array antenna," *IEEE Trans. Antennas Propag*., vol. 61, no. 5, pp. 2482–2489, May 2013.

[8] M. G. N. Alsath and M. Kanagasabai, "Ultra-wideband grid array antenna for automotive radar sensors," *IET Microw. Antennas Propag*., vol. 10, no. 15, pp. 1613–1617, Jun. 2016.

[9] L. Zhang, W. Zhang, and Y. P. Zhang, "Microstrip grid and comb array antennas," *IEEE Trans. Antennas Propag*., vol. 59, no. 11, pp. 4077–4084, Nov. 2011.

[10] H. Nakano, Y. Iitsuka, and J. Yamauchi, "Loop-based circularly polarized grid array antenna with edge excitation," *IEEE Trans. Antennas Propag*., vol. 61, no. 8, pp. 4045–4053, Aug. 2013.

[11] M. G. N. Alsath, L. Lawrance, and M. Kanagasabai, "Bandwidth-enhanced grid array antenna for UWB automotive radar sensors," *IEEE Trans. Antennas Propag*., vol. 63, no. 11, pp. 5215–5219, Nov. 2015.

[12] E. Arnieri, F. Greco, L. Boccia, and G. Amendola, "A reduced size planar grid array antenna for automotive radar sensors," *IEEE Antennas Wireless Propag. Lett.*, vol. 17, no. 12, pp. 2389–2393, Dec. 2018.

[13] Z. Chen, L. Zhang, B. Zhang, and Y. P. Zhang, "A multiport microstrip grid array structure," *IEEE Trans. Antennas Propag*., vol. 64, no. 11, pp. 4953–4958, Nov. 2016.

[14] T. Zhihong, Y. P. Zhang, C. Luxey, A. Bisognin, D. Titz, and F. Ferrero, "A ceramic antenna for tri-band radio devices," *IEEE Trans. Antennas Propag*., vol. 61, no. 11, pp. 5776-5780, Nov. 2013.

[15] B. Zhang and Y. P. Zhang, "Grid array antennas with subarrays and multiple feeds for 60-GHz radios," *IEEE Trans. Antennas Propag*., vol. 60, no. 5, pp. 2270–2275, May 2012.

[16] M. Sun, Y. P. Zhang, D. Liu, K. M. Chua, and L. L. Wai, "A ball grid array package with a microstrip grid array antenna for a single-chip 60-GHz receiver," *IEEE Trans. Antennas Propag*., vol. 59, no. 6, pp. 2134–2140, Jun. 2011.

[17] Y. P. Zhang, M. Sun, D. Liu, and Y. Lu, "Dual grid array antennas in a thin-profile package for flip-chip interconnection to highly integrated 60-GHz radios," *IEEE Trans. Antennas Propag*., vol. 59, no. 4, pp. 1191–1199, Apr. 2011.

[18] Z. Chen, Y. P. Zhang, A. Bisognin, D. Titz, F. Ferrero, and C. Luxey, "An LTCC microstrip grid array antenna for 94-GHz applications," *IEEE Antennas Wireless Propag. Lett.*, vol. 14, pp. 1279–1281, 2015.

[19] Z. Chen, Y. P. Zhang, A. Bisognin, D. Titz, F. Ferrero, and C. Luxey, "A 94-GHz dual-polarized microstrip mesh array antenna in LTCC technology," *IEEE Antennas Wireless Propag. Lett.*, vol. 15, pp. 634–637, 2016.

[20] J. D. Hughes, C. Occhiuzzi, J. Batchelor, and G. Marrocco, "Twin-grid array as 3.6 GHz epidermal antenna for potential backscattering 5G communication," *IEEE Antennas Wireless Propag. Lett.*, vol. 19, no. 12, pp. 2092–2096, Dec. 2020.

[21] L. Zhang, K. Y. See, B. Zhang, and Y. P. Zhang, "Integration of dual-band monopole and microstrip grid array for single-chip tri-band application," *IEEE Trans. Antennas Propag*., vol. 61, no. 1, pp. 439–443, Jan. 2013.

[22] G. Xu, H. Peng, Z. Shao, L. Zhou, Y. Zhang, and W. Yin, "Dual-band differential shifted-feed microstrip grid array antenna with two parasitic patches," *IEEE Trans. Antennas Propag.*, vol. 68, no. 3, pp. 2434–2439, Mar. 2020.

[23] R. W. Ziolkowski, P. Jin, and C. Lin, "Metamaterial-inspired engineering of antennas," *Proc. IEEE*, vol. 99, no. 10, pp. 1720-1731, Oct. 2011.

[24] M.-C. Tang, B. Zhou, Y. Duan, X. Chen, and R. W. Ziolkowski, "Pattern-reconfigurable, flexible, wideband, directive, electrically small near-field resonant parasitic antenna," *IEEE Trans. Antennas Propag.*, vol. 66, no. 5, pp. 2271–2280, May 2018.

[25] M.-C. Tang, Z. Wu, T. Shi, and R. W. Ziolkowski, "Dual-band, linearly polarized, electrically small Huygens dipole antennas," *IEEE Trans. Antennas Propag.*, vol. 67, no. 1, pp. 37–47, Jan. 2019.

[26] M.-C. Tang, Q. Lin, M. Li, and R. W. Ziolkowski, "Polarization-reconfigurable Yagi-configured electrically small antenna," *IEEE Trans. Antennas Propag.*, vol. 69, no. 3, pp. 1757–1762, Mar. 2021.

[27] S. M. A. M. H. Abadi, J. H. Booske, and N. Behdad, "Exploiting mechanical flexure as a means of tuning the responses of large-scale periodic structures," *IEEE Trans. Antennas Propag.*, vol. 64, no. 3, pp. 933–943, Mar. 2016.

[28] A. Kianinejad, Z. N. Chen, and C. W. Qiu, "Design and modeling of spoof surface plasmon modes-based microwave slow-wave transmission line," *IEEE Trans. Microw. Theory Techn.*, vol. 63, no. 6, pp. 1817–1825, 2015.

[29] A. E. Ruehli, "Inductance calculations in a complex integrated circuit environment," *IBM J. Res. Develop*., vol.16, no.5, pp.470–481, Sep. 1972.

[30] R. T. Cutshall and R. W. Ziolkowski, "Performance characteristics of planar and three-dimensional versions of a frequency-agile electrically small antenna," *IEEE Antennas Propag. Magazine*, vol. 56, no. 6, pp. 53–71, Dec. 2014.

[31] K. Wei, Z. Zhang, Z. Feng and M. F. Iskander, "A wideband MNG-TL dipole antenna with stable radiation patterns," *IEEE Trans. Antennas Propag.*, vol. 61, no. 5, pp. 2418–2424, May 2013.

[32] W. Hu, X. Liu, S. Gao, L. Wen, Q. Luo, P. Fei, Y. Yin, and Y. Liu, "Compact wideband folded dipole antenna with multi-resonant modes," *IEEE Trans. Antennas Propag.*, vol. 67, no. 11, pp. 6789–6799, Nov. 2019.

[33] Y. Luo, X. Ma, N. Yan, W. An, and K. Ma, "Sidelobe suppression of dual-mode compressed high-order-mode dipole by loading bent stubs," *IEEE Antennas Wireless Propag. Lett.*, vol. 20, no. 6, pp. 898–902, Jun. 2021.

[34] K. V. Puglia, "Electromagnetic simulation of some common balun structures," *IEEE Microw. Mag.*, vol. 3, no. 3, pp. 56–61, Sep. 2002.

[35] S. A. Saario, J. W. Lu, and D. V. Thiel, "Full-wave analysis of choking characteristics of sleeve balun on coaxial cables," *Electron. Lett*., vol. 38, no. 7, pp. 304–305, Mar. 2002.

[36] *SG128 Multi-Probe Antenna Measurement System*. [Online]. Available:https://www.mvg-world.com/en/system/files/datasheet_sg128_bd.pdf.

[37] OSD/DARPA, Ultra-Wideband Radar Review Panel, "Assessment of ultra wide-band (UWB) technology", Arlington, VA, Defense Advanced Research Project Agency (DARPA), 1990.

[38] Federal Communications Commission, "First report and order in the matter of revision of part 15 of the commission's rules regarding ultra-wideband transmission systems," ET Docket 98-153, FCC 02-48, released Apr 22, 2002.

[39] D. Wen, Y. Hao, H. Wang, and H. Zhou, "Design of a wideband antenna with stable omnidirectional radiation pattern using the theory of characteristic modes," *IEEE Trans. Antennas Propag*., vol. 65, no. 5, pp. 2671–2676, May 2017.

[40] Y. Luo and Z. N. Chen, "Compressed dipoles resonating at higher order modes with enhanced directivity," *IEEE Trans. Antennas Propag*., vol. 65, no. 11, pp. 5697–5701, Nov. 2017.

[41] Y. Luo, Z. N. Chen, and K. Ma "Enhanced bandwidth and directivity of a dual-mode compressed high-order mode stub-loaded dipole using characteristic mode analysis," *IEEE Trans. Antennas Propag*., vol. 67, no. 3, pp. 1992–1925, Mar. 2019.

[42] Y. Yang, Z. Li, S. Wang, X. Chen, J. Wang, and Y. J. Guo, "Miniaturized high-order-mode dipole antennas based on spoof surface plasmon polaritons," *IEEE Antennas Wireless Propag. Lett*., vol. 17, no. 12, pp. 2409–2413, Dec. 2018.